Photoacoustic Imaging of Nanoparticle-Containing Cells Using Single-Element Focused Transducer: A Simulation Study

Subhajit Karmakar, Madhusudan Roy, and Ratan K. Saha

***Abstract*—A new theoretical approach for photoacoustic (PA) image simulation of an ensemble of cells with endocytosed gold nanoparticles is presented. Each cell was approximated as a fluid sphere and suspended in a nonabsorbing fluid medium. It was assumed that the cellular optical absorption coefficient changed greatly because of endocytosis of nanoparticles; however, thermophysical parameters remained unchanged because nanoparticles occupied negligible intracellular volume. A frequency-domain method was used to obtain a PA signal from a single cell and resultant signal detected by a focused single-element transducer was evaluated by convolving signals from many cells with the spatial impulse response function of the receiver. The proposed model was explored to simulate PA images of numerical phantoms. It was observed that features of the phantoms are retained precisely in those simulated images. Also, speckles in PA images are significantly suppressed because of strong boundary buildup when cells are bounded to a region. Nevertheless, speckle visibility increases when cells are not bounded to a region. This approach may be developed as a realistic simulation tool for PA imaging of tissue medium utilizing its cellular feature.**

I. Introduction

The photoacoustic (PA) effect—generation of sound waves resulting from absorption of light—was discovered by Alexander Graham Bell in 1880. However, it was in the late 1990s when initiatives were taken to develop an imaging modality by exploiting this effect for biomedical applications, and, in fact, major advancements took place over the last decade [1]–[3]. The PA imaging technique has gained attention because it combines the most compelling properties of optics and acoustics. For example, a PA image can faithfully display high optical contrast possessed by biological tissue. This is possible because, by choosing suitable incident wavelengths, optical absorption by tissue endogenous chomophores can be maximized with respect to its nonabsorbing components. Further, because scattering of sound waves is two to three orders of magnitude less than that of light, this method can form images at depths where other optical modalities (such as confocal microscopy, two-photon microscopy, etc.) do not work. The PA technique provides images at ultrasonic resolution and hence, by selecting appropriate transducers, biological structures of different scales can be visualized. In addition to anatomical imaging, functional information can also be gathered by measuring PA signals at multiple optical wavelengths followed by a spectroscopic analysis, which may become invaluable for studying various biological processes of interests.

Currently, PA imaging techniques have been extensively explored at two settings, namely, photoacoustic microscopy (PAM) and photoacoustic tomography (PAT). For PAM, a confocal geometry is generally used to weakly focus the laser beams into the tissue situated at the focal region of the acoustic detector. The laser–transducer module performs a raster scan to capture PA signals and an image is generated using those raw signals [2]. Zhang *et al.*, using a 50-MHz transducer, produced longitudinal image of tumor angiogenesis in rats *in vivo* for 584 and 764 nm illuminations [2]. The PAM technique has also been used to generate images of cells and small animal organs by other investigators [4], [5]. For PAT, the imaging region is uniformly irradiated and PA signals are detected using either linear or circular-array transducers [3]. The recorded signals are then back-projected to reconstruct a high-resolution image. Wang and Hu were able to image breast vasculature in a human volunteer *in vivo* using a linear array operating in a frequency band of 4 to 8 MHz [3]. The implication of obtaining PA images with ultrasound (US) transducers in the diagnostic frequency range (2 to 15 MHz) is likely to be far reaching. It essentially motivates development of a dual-modality US and PA system for clinical applications. Such a system should noninvasively provide both anatomical and functional information of the imaging region in a co-registered manner [6]. Several attempts have been made by various research groups to achieve this end [7]–[11]. The capability of PA imaging specifically for *in vivo* applications can be improved further by introducing contrast agents [12]. Various metallic and nonmetallic nanoparticles (NPs) have been used as contrast agents in many studies [13]–[16]. For example, gold NPs (AuNPs) were used as a contrast agent for imaging cancer cells [13]–[15] and carbon nanotubes were administered for visualizing tumors in a small animal model [16].

Besides experimental investigations, efforts have also been made to study spatial and temporal variation of

Manuscript received October 18, 2014; accepted November 27, 2014. R. K. Saha expresses his thanks to the Council of Scientific and Industrial Research (CSIR), New Delhi, India, for funding.

S. Karmakar is with the University Science Instrumentation Centre, The University of Burdwan, Bardhaman, West Bengal, India.

M. Roy and R. K. Saha are with the Surface Physics and Material Science Division, Saha Institute of Nuclear Physics, 1/AF Bidhannagar, Kolkata, India (e-mail: ratank.saha@saha.ac.in).

DOI http://dx.doi.org/10.1109/TUFFC.2014.006786

PA fields generated by regular objects (e.g., cylinders, spheres, etc.) as well as biological structures (e.g., vascular networks) through computer simulations [17]. The k-Wave simulation tool box has been exclusively used for this purpose. It numerically solves coupled partial differential equations of fluid dynamics in an elegant manner. It calculates spatial derivatives using the Fourier transform method and temporal derivatives using a time propagator. This approach provides accurate time evolution even for larger time steps and thus reduces computational burden. The k-Wave method has been found to be immensely useful for optimizing various parameters (such as laser arrangement and pulse length, receiver arrangement and bandwidth, etc.) and to study the performance of reconstruction algorithms for PAT applications [18], [19]. However, in many situations, the whole field at every time step must be computed to obtain acoustic pressure time-series data at a single point [17]. Moreover, the existing studies based on this tool box modeled tissue as a homogeneous distribution of chromophores, and therefore the cellular aspect of tissue was neglected.

The PA field generated by a cell, approximated as a fluid sphere packaging chromophores and suspended in a nonabsorbing fluid medium, can be calculated by solving a wave equation in the frequency domain with the use of appropriate boundary conditions [20]. The time-domain solution can readily be obtained by employing the inverse Fourier transformation. The inherent assumption of this formulation is that light absorption takes place at the molecular level but acoustic emission takes place at the cellular level. The PA field from many cells can be expressed as a linear superposition of fields emitted by the individual cells [21]. This is known as the single-particle approach and has been successfully utilized to explain experimental results in ultrasonic and optical scattering problems [22], [23]. This theoretical model has been used to predict the PA behavior of non-aggregated and aggregated red blood cells [21] and was subsequently compared with experimental results [24]. It has been employed to study the PAs of oxygenated and deoxygenated red blood cells, malaria infected erythrocytes, melanoma cells in blood, and as also cancer cells with endocytosed AuNPs [25]–[28].

In this paper, the solution to the PA wave equation for a spherical source and the spatial impulse response function (SIRF) are combined to derive an analytical expression of the PA signal for a focused single-element transducer receiving tiny signals from a collection of cells with endocytosed AuNPs. It has been hypothesized that endocytosed AuNPs alter cellular optical absorption property in a significant manner, although thermophysical parameters of cells remain unchanged because AuNPs occupy a negligible intracellular volume. The SIRF relates transducer geometry to the transmit/receive field and can be evaluated by computing pressure signal detected by the receiver for a delta function disturbance originated by a point source [29]. It may be noted that a cell emits an acoustic pulse of finite width when uniformly illuminated by a delta function laser pulse. Therefore, the PA signal detected by a transducer for a single PA source can be expressed in terms of convolution between the emitted acoustic pulse and the SIRF. For many particle systems, the resultant PA signal can be obtained by linearly adding those signals from individual cells. The detailed derivation of the model is presented in Section II. Such a framework has been explored in this work to simulate B-mode images of numerical phantoms containing cells loaded with AuNPs. The simulation method is illustrated in Section III. The simulated results are presented in Section IV. Finally, Section V contains discussion and conclusions of this work.

II. Mathematical Framework

A. Modeling of PA Field From a Single Spherical Source

The time-dependent wave equation for the PA field can be derived from the linearized equations of fluid dynamics using the condition of thermal confinement. It is given by [20]

$$\nabla^2 p - \frac{1}{v_s^2}\frac{\partial^2 p}{\partial t^2} = -\frac{\beta}{C_P}\frac{\partial Q}{\partial t}. \tag{1}$$

Here, v_s, β, and C_P are the acoustic wave velocity, thermal expansion coefficient, and isobaric specific heat for the light-absorbing region, respectively; Q is the amount of heat received by the absorbing region per unit time per unit volume. If an intensity-modulated laser beam with intensity I_0 and modulation frequency ω is used to deliver heat, (1) reduces to its time-independent form as [20]

$$\nabla^2 p + k^2 p = \begin{cases} \dfrac{i\omega\mu\beta I_0}{C_P} & \text{inside the absorber} \\ 0 & \text{outside the absorber}, \end{cases} \tag{2}$$

where μ is the optical absorption coefficient for the absorber. Eq. (2) can readily be solved in spherical polar coordinates for a spherical absorber of radius a using appropriate boundary conditions (such as the continuity of pressure field and continuity of the normal component of the particle velocity at the spherical boundary). The solution to (2) becomes [20]

$$p(\mathbf{r}', \omega) = BI_0 p_n(\omega)\frac{e^{ik_f|\mathbf{r}'-\mathbf{r_n}|}}{|\mathbf{r}'-\mathbf{r_n}|}, \tag{3}$$

where $|\mathbf{r}' - \mathbf{r_n}|$ is the distance between the observation point $\mathbf{r}'$ and the center of the nth absorber positioned at $\mathbf{r_n}$ as shown in Fig. 1, $B = (i\mu\beta v_s a^2)/C_P$, and

$$p_n(\omega) = \frac{j_1(\hat{q})e^{-ik_f a}}{\left[(1-\hat{\rho})\frac{\sin(\hat{q})}{\hat{q}} - \cos(\hat{q}) + i\hat{\rho}\hat{v}\sin(\hat{q})\right]}, \tag{4}$$

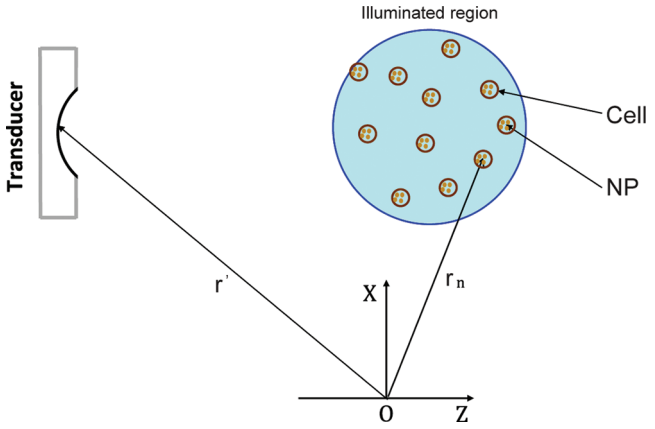

Fig. 1. Basic geometry of the imaging system.

with $\hat{q} = k_s a$. The notation j_1 represents the spherical Bessel function of the first kind of order unity. The dimensionless quantities $\hat{\rho} = \rho_s/\rho_f$ and $\hat{v} = v_s/v_f$ indicate the density and the acoustic wave velocity for the absorber with respect to those for the suspending medium, respectively; k_s and k_f are the wave numbers for the acoustic wave inside and outside the source, respectively. The time-dependent PA field for a delta function heating pulse can be derived by taking the inverse Fourier transform of (3), yielding [20]

$$p(\mathbf{r}', t) = \frac{BF}{2\pi}\int_{-\infty}^{\infty} \mathrm{d}\omega p_n(\omega)\frac{e^{ik_f|\mathbf{r}'-\mathbf{r_n}|}}{|\mathbf{r}'-\mathbf{r_n}|}e^{-i\omega t}, \tag{5}$$

where F is the incident fluence and (5) denotes an analytic signal. It may also be noted that contributions from all possible frequencies are summed up while calculating PA signal, so it is a wide bandwidth signal.

B. Modeling of PA Signal Detected by a Focused Single-Element Transducer

The measured signal $p_n^{\mathrm{m}}(\omega)$ for the nth source is proportional to PA pressure spatially averaged over the surface S of the transducer and it can be written as

$$\begin{aligned} p_n^{\mathrm{m}}(\omega) &\approx \frac{2\pi}{S_A} BI_0 p_n(\omega)\int_S \frac{e^{ik_f|\mathbf{r}'-\mathbf{r_n}|}}{2\pi|\mathbf{r}'-\mathbf{r_n}|}\,\mathrm{d}^2\mathbf{r}', \\ &= \frac{2\pi}{S_A} BI_0 p_n(\omega) H_D(\mathbf{r}_n, \omega), \end{aligned} \tag{6}$$

where S_A is the aperture area and $H_D(\mathbf{r_n}, \omega) = \int_S (e^{i\omega/v_f|\mathbf{r}'-\mathbf{r_n}|})/(2\pi|\mathbf{r}'-\mathbf{r_n}|)\mathrm{d}^2\mathbf{r}'$ is the directivity function of the transducer [29].

The equivalent time-domain expression $p_n^{\mathrm{m}}(t)$ can be obtained by taking the inverse Fourier transform of the previous equation, and can be expressed as

$$p_n^{\mathrm{m}}(t) = \frac{2\pi}{S_A}[p_n(t) *_t h(\mathbf{r_n}, t)], \tag{7}$$

where

$$p_n(t) = \frac{BF}{2\pi}\int_{-\infty}^{\infty} \mathrm{d}\omega p_n(\omega) e^{-i\omega t}, \tag{8}$$

$*_t$ denotes temporal convolution, and $h(\mathbf{r_n}, t) = \int_S \delta(t - |\mathbf{r}' - \mathbf{r_n}|/v_f)/(2\pi|\mathbf{r}' - \mathbf{r_n}|)\mathrm{d}^2\mathbf{r}'$ represents the SIRF of the acoustic receiver. The measured PA signal $P(t)$ for a collection of monodisperse absorbers with similar biophysical and biochemical conditions can be cast as a linear superposition of the tiny signals emitted by the individual sources,

$$P(t) = \sum_{n=1}^{N} p_n^{\mathrm{m}}(t). \tag{9}$$

The corresponding geometry is displayed in Fig. 1. In practice, PA pressure signals are real and detected by an ultrasound transducer with finite receiving bandwidth. A Gaussian function can be used to suitably model the frequency response of such a transducer. Therefore, a complex filtering function can be constructed with real and imaginary parts as

$$g_R(\omega_0, \xi, t) = \frac{\xi}{\sqrt{2\pi}} e^{-(\xi^2 t^2)/2}\cos(\omega_0 t), \tag{10}$$

$$g_I(\omega_0, \xi, t) = \frac{\xi}{\sqrt{2\pi}} e^{-(\xi^2 t^2)/2}\sin(\omega_0 t), \tag{11}$$

where ω_0 is the center frequency and ξ is the -6-dB bandwidth of the Gaussian function. A bandlimited (BL) RF line $P_R^{\mathrm{BL}}(t)$ can be formed by convoluting the real part of $P(t)$ with g_R as [26]

$$P_R^{\mathrm{BL}}(t) = \mathrm{Re}\{P(t)\} *_t g_R(\omega_0, \xi, t). \tag{12}$$

The Hilbert transform of (12) can be illustrated as [26]

$$P_I^{\mathrm{BL}}(t) = \mathrm{Re}\{P(t)\} *_t g_I(\omega_0, \xi, t). \tag{13}$$

The envelope $E(t)$ of RF line can be evaluated using the following operation:

$$E(t) = \sqrt{(P_R^{\mathrm{BL}}(t))^2 + (P_I^{\mathrm{BL}}(t))^2}. \tag{14}$$

In this work, (14) was computed to simulate the PA amplitude line (A-line) for an ensemble of randomly positioned cells when detected by a focused transducer.

III. Methods

A. Parameter Selection

In this study, each cell was considered as a fluid sphere with radius $a = 5$ μm which mimicked human epithelial carcinoma cells (A431 keratinocyte). This cell line was

previously imaged by others [13]. These cells encapsulated Au nanospheres with radius 25 nm. The plasmon resonance peak for such NPs appears around 520 nm, where light absorption is maximum. The absorption coefficient for a cell enclosing AuNPs could be estimated by multiplying the intracellular concentration of NPs with its absorption cross-section at the wavelength of interest, i.e., $\mu = C_{\mathrm{NP}}\sigma_{\mathrm{abs}}$. The intracellular concentration of NPs was determined as C_{NP} = number of NPs divided by the volume of a cell and absorption cross-section was obtained from σ_{abs} = product of absorption efficiency and geometrical cross-section of an NP. The absorption efficiency for NPs was calculated using the Mie theory [30]. This theory describes scattering and absorption of electromagnetic radiation by a spherical particle of arbitrary size. It solves the Maxwell equations in spherical polar coordinates and uses appropriate boundary conditions at the surface of the spherical object to derive exact analytical expressions for extinction, scattering, and absorption cross-sections. In this work, real and imaginary parts of the refractive index at different optical wavelengths for Au were taken from literature, and those numerical values were utilized in computing the cross-sections [31]. The absorption efficiency was computed as 3.297 at 532 nm, and accordingly, μ was found to be 56 004.65 cm^{-1} for a typical intracellular concentration of NPs of about 45.3×10^4 NPs/cell [28]. Previously, experiments were performed with cells containing NPs at this concentration [14].

The density and the speed of sound for cell were chosen as $\rho_{\mathrm{s}} = 1090$ kg/m^3 and $v_{\mathrm{s}} = 1535$ m/s, respectively [32]. These numerical values are similar to those of acute myeloid leukemia cells. Other quantities, such as thermal expansion coefficient, isobaric specific heat, and fluence of the optical beam, were taken as constant because these parameters essentially control amplitude of the signal and do not affect its frequency content. The density and the speed of sound for the surrounding medium were fixed at $\rho_{\mathrm{f}} = 1005$ kg/m^3 and $v_{\mathrm{f}} = 1540$ m/s, respectively [22].

B. Phantom Generation

1) Cyst Phantom: A numerical phantom was constructed using NP-filled cells which were randomly positioned inside the volume of $20 \times 0.7 \times 25$ mm^3. The volume fraction occupied by cells was 20×10^4 cells/mL, which was similar to that of experiments in [13] and [14]. The random positioning of non-overlapping spheres in 3-D is generally computationally expensive. However, an algorithm was developed employing the Monte Carlo technique to simulate tissue realizations in 3-D within realistic time frame. A detailed description of the algorithm is presented in [26]. Briefly, the entire volume was divided into several boxes of size $0.5 \times 0.07 \times 25$ mm^3. Each box was separately filled with spheres in such a way so that they did not overlap. Further, spheres situated at the boundaries of a box also maintained non-overlapping condition with particles from other boxes. A simulated tissue configuration composed of spatially random distribution of cells is shown in Fig. 2(a). All cells in this figure had $\mu =$ 56 004.65 cm^{-1} except those located within the spherical regions [see Fig. 2(a)]. The cellular absorption coefficient for cells inside the spherical regions on the left side was set to be 30 dB less (i.e., $\mu = 1771.02$ cm^{-1} and 1.4×10^4 NPs/cell) than that of cells outside the spheres. However, it was 30 dB higher (i.e., $\mu = 1771022.50$ cm^{-1} and 1432.5×10^4 NPs/cell) for cells belonging to the spherical regions on the right side compared with that of cells outside the spheres. The spherical regions on the left and right sides of Fig. 2(a) had diameters of 7.0, 5.0, and 3.0 mm from top to bottom, respectively. The PA image simulation methodology is described later and a side view of the scanning geometry for this phantom is shown in Fig. 2(b).

2) Staircase Phantom: Another numerical phantom was simulated and the corresponding PA image was generated. In this case, the entire volume (i.e., $20 \times 0.7 \times 25$ mm^3) was divided into four regions along the x-direction, as shown in Fig. 3(a), and populated with cells having different absorption coefficients such that they formed absorption stair steps. The absorption coefficient for cells in the third stair (from the left) was about 56 004.65 cm^{-1}, whereas the same in the two stairs on the left and one on the right was at -20, -10, and 10 dB with respect to the third one, respectively. Accordingly, intracellular NP concentration could be calculated to be 4.5×10^4, 14.3×10^4, 45.3×10^4, and 143.2×10^4 NPs/cell from left to right. It might be noted that the darkness of circles mimicking cells gradually increased from left to right in Fig. 3(a), indicating sequential increment of μ.

C. PA Image Formation

A side view of the scanning geometry is shown in Figs. 2(b) and 3(a). A 532-nm laser beam propagated along the y-direction and uniformly illuminated a volume of $0.5 \times 0.7 \times 25$ mm^3 containing 1750 cells. The irradiated region is highlighted in each figure. PA waves emitted by cells belonging to that irradiated volume and propagated along the $-z$-direction were detected employing a focused transducer. A scan line was constructed by summing the tiny signals from those cells. Initially, 40 scan lines along the x-direction were generated from the entire phantom (i.e., $20 \times 0.7 \times 25$ mm^3). The diameter of the transducer was 8 mm with 20 mm as the focal length. The SIRF of such a receiver could be evaluated by computing the analytical expression of the SIRF of a concave spherical radiator originally derived by Arditi *et al.* [33]. However, in this work, Field II [29] was used to calculate the SIRF of the transducer and the PA pressure field from cells was obtained by evaluating (9). The sampling rate was fixed at 4 GHz. The BL RF lines from the wideband pressure signal were obtained for three transducers (center frequencies at 10, 25, and 50 MHz and 60% bandwidth at -6 dB for each). The envelope of each BL signal was determined using the Hilbert transform pairs and calculating (14). The Gaussian window of the filtering functions was

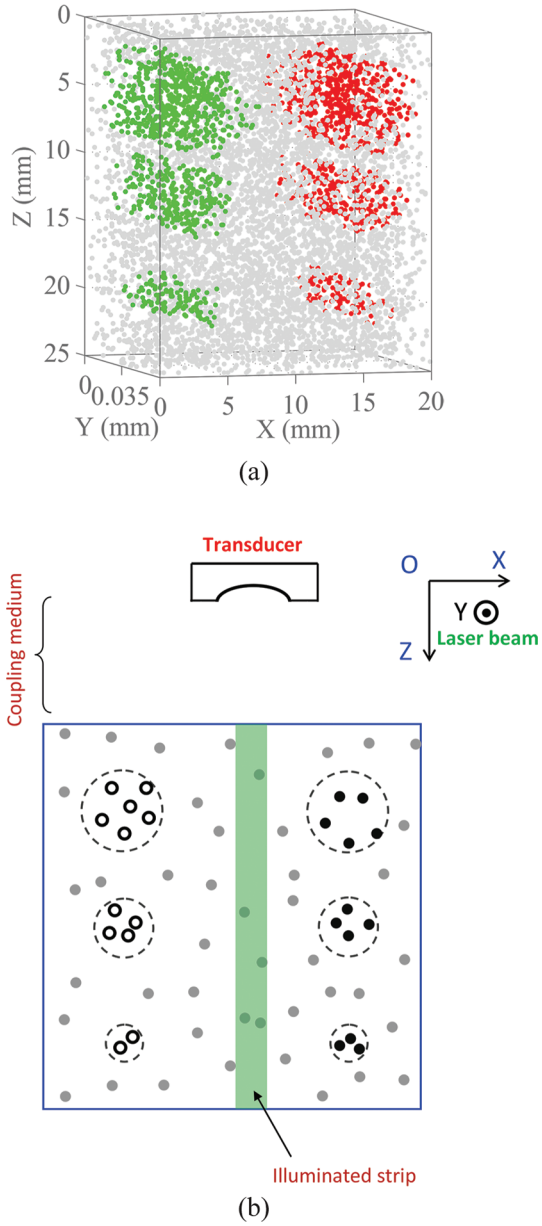

Fig. 2. (a) A numerical phantom consists of randomly positioned cells containing NPs at three different concentrations. Cells (green spheres) within three spherical regions at the left contain about 1.4×10^4 NPs/cell, whereas the cells (red spheres) in the regions at the right contain about 1432×10^4 NPs/cell. The remaining cells (gray spheres) enclose 45.3×10^4 NPs/cell. (b) Side view of the scanning geometry.

truncated to $\pm 4/\xi$ length. Each BL RF line was further downsampled by a factor of 100 and log compression was used to obtain a finite dynamic range B-mode PA image. Log-compressed RF lines were then interpolated 13 times along the x-direction employing a cubic interpolator to generate the final 50 dB dynamic range B-mode PA image of the numerical phantom and 256 gray levels were used to encode the dynamic range. The calculation of SIRFs for many cells is a computationally expensive task in this approach. For example, it took about 8 h in a personal computer [OS: Windows 7 (Microsoft Corp., Redmond, WA); Processor: Intel Core i3–2130 CPU (Intel Corp., Santa Clara, CA), 3.40 GHz; RAM: 4 GB] to generate a PA image of a region with 70 000 cells using a focused transducer with 8 mm diameter and 20 mm as the focal length.

D. Speckles in PA Imaging

The origin to speckles in PA images was also studied in this work in detail. For this purpose, a phantom was generated. It was a kind of agar-gelatin block with size $3 \times 0.05 \times 3$ mm^3. It contained a cylindrical region with an axis of symmetry along the y-direction [see Fig. 3(b)]. It was populated with cells enclosing AuNPs. The radius and height of the cylinder were 1000 and 50 μm, respectively. The volume fraction occupied by cells inside the cylindrical region was varied from 10% to 40% with a 10% increment; however, cell concentration outside the cylindrical region was zero. A 2-D view of such a phantom is shown in Fig. 3(b). A representative illuminated region is also shown in this figure. PA signals for such samples were computed and analyzed to examine how cell concentration affected boundary buildup and speckle visibility. To study these effects further, another type of sample was investigated. In this case, the volume fraction occupied by cells inside the cylindrical region was kept constant at 20% but it was gradually changed from 0 to 10% outside that volume. In both cases, cells were loaded with NPs at a concentration of 45.3×10^4 NPs/cell, providing $\mu = 56\,004.65$ cm^{-1}. Finally, the effect of intracellular NP concentration on speckles in PA images was examined. In this case, cell concentrations inside and outside the cylindrical region were fixed at 20%. The intracellular NP concentration for cells inside the cylindrical region was taken as 45.3×10^4 NPs/cell. The concentration was decreased from 18.1×10^4 to 2.3×10^4 for cells outside that region so that contrast (defined as the ratio of optical absorption coefficient for cells inside to outside the cylindrical region) increased approximately from 2.5 to 20.

IV. Results

B-mode images of the phantom depicted in Fig. 2 are shown in Fig. 4. Three images have been generated at three different center frequencies of the ultrasound transducer [see Figs. 4(a)–4(c) for 10, 25, and 50 MHz, respectively]. Fig. 4(a) demonstrates that six spherical regions appeared at the desired locations with expected sizes and shape. This served as a code sanity cheek. Although optical absorption for cells within three spherical regions on the right side of the cyst phantom (see Fig. 2) is identical, the middle circle in the PA image looks much brighter than the other two positioned above and below it. The central region of the cyst phantom falls inside the depth of field of the transducer that has a focal length of 20 mm. PA signals from cells located within the depth of field because of focusing action are added constructively, producing large intensity in the brightness map. Similarly, some bright spots are visible inside the middle circle on the left side. Other circles appear to be dark and textureless

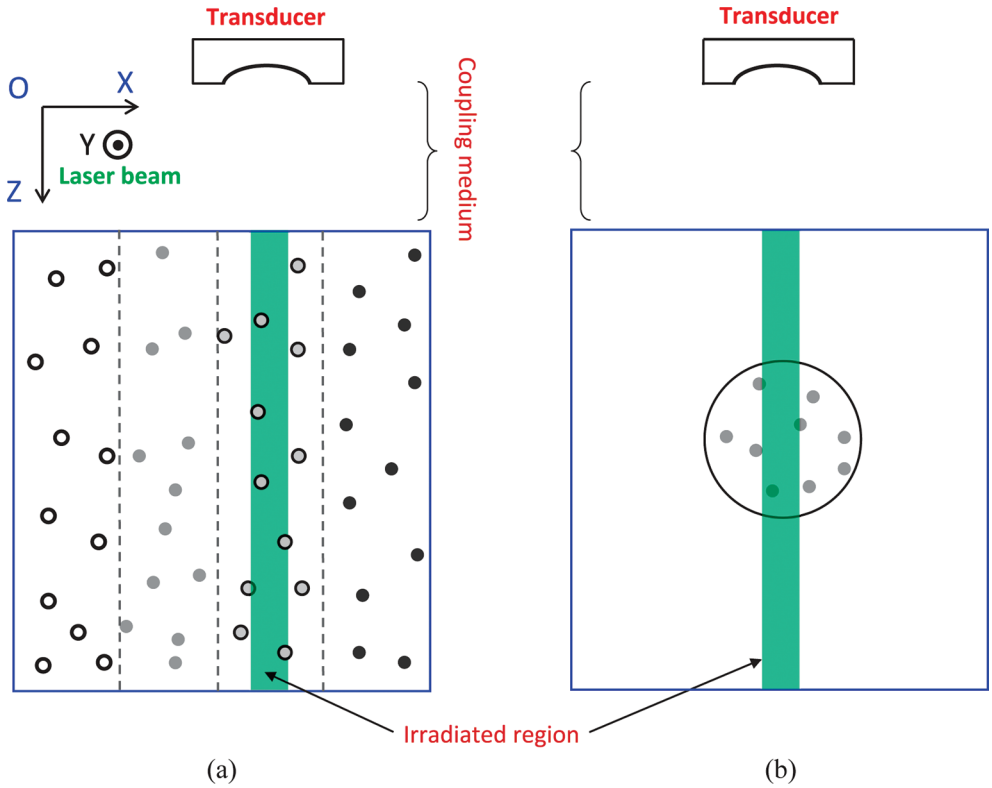

Fig. 3. (a) Side view of the scanning geometry for the staircase phantom. It contains four boxes. The intracellular NP concentrations are 4.5×10^4, 14.3×10^4, 45.3×10^4, and 143.2×10^4, from left to right. Accordingly, μ is 5563.37, 17679.17, 56004.65, and 177038.98 cm^{-1}, respectively. (b) Same as (a) but for the first type of speckle phantoms. Endocytosed cells are present within the cylindrical volume at the central region of the phantom. For other types of phantoms, cells exist outside the cylindrical region as well.

because they are situated away from the focus. Note that these circles confine cells having identical light absorption coefficients. Similar observations can also be made from Figs. 4(b) and 4(c). However, as expected, the size of the focal region has shrunk as the center frequency of the transducer is increased. Moreover, the number of bright pixels inside each circular region decreases with increasing center frequency and, hence, brightness and contrast of that circular area are reduced with respect to the background. This may be attributed to the fact that sharp and narrow N-shaped pressure pulses emitted by a single cell become flat when filtered by a low-frequency transducer (e.g., 10 MHz) and consequently, the number of pixels with intermediate gray values increases. Some dark spots have appeared at the focus in Fig. 4(c) but those are not present in Fig. 4(a). The white arrow in Fig. 4(c) indicates a dark spot. It may be noted that a sparse medium ($\approx$0.01% being the volume fraction occupied by cells) has been imaged and those dark spots may correspond to non-absorbing extracellular matrix appearing, particularly at higher frequencies.

Fig. 5(a) displays a simulated PA image of the staircase phantom for a 10-MHz transducer. Corresponding images simulated at 25 and 50 MHz are depicted in Figs. 5(b) and 5(c), respectively. Fig. 5(a) illustrates that only the focal region is visible in the leftmost strip. However, the visible region gets gradually extended from left to right because of increasing intracellular NP concentration enhancing PA signals from cells. Figs. 5(b) and 5(c) also exhibit similar variation. Similar to the previous case, some dark spots are specified with white arrows in Figs. 5(b) and 5(c). Plots of average PA amplitude as a function of NP concentration are shown in Fig. 6 at three center frequencies. The NPs reside within cells. The mean PA amplitude has been calculated by averaging signals over an area of 4×10 mm^2 on each staircase [see Fig. 5]. The linear variation is expected because PA amplitude in this model follows a linear relationship with μ [see (3)].

It is evident from Figs. 4 and 5 that fully developed speckles are present in these simulated images. To investigate the origin of speckles in PA images, a detailed study has been performed in this work. For this purpose, three types of phantoms were constructed and imaged via *in silico* experiments as discussed in Section III-D. We begin with three representative A-lines corresponding to the central region of those samples, as plotted in Fig. 7. The upper panel of Fig. 7 shows the A-line for a sample in which 20% of the volume inside the cylindrical region is filled by cells having the same μ values and no cells are present outside this region. The middle panel of Fig. 7 is generated from a sample for which cells occupy 20% of the volume inside the cylindrical region; however, they occupy 5% outside. For both the regions, μ is constant. The lower panel corresponds to a sample for which 20% of the volume both inside and outside of the cylinder is taken up by cells but contrast is about 2.5. It can be seen from

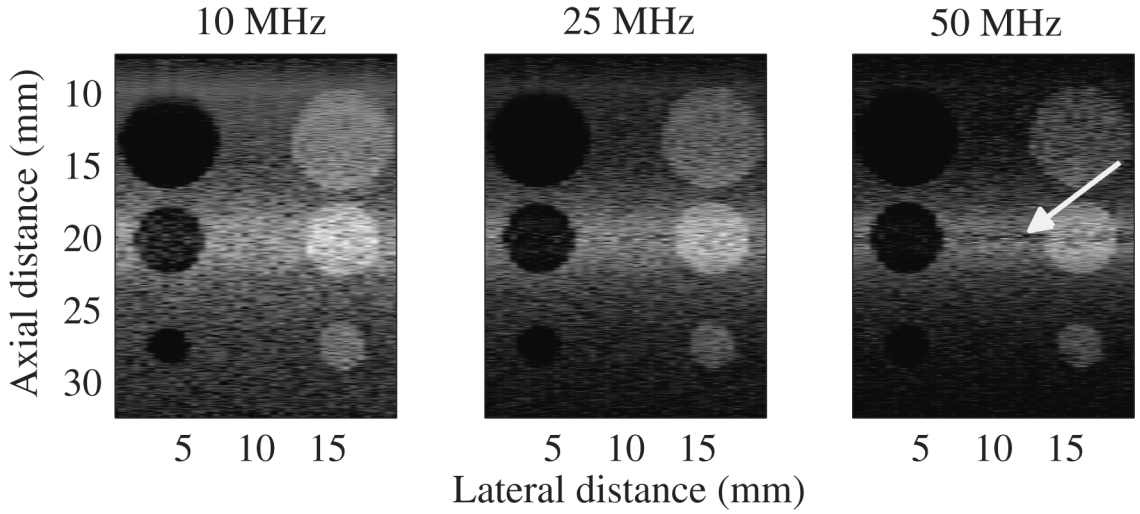

Fig. 4. (a)–(c) 50 dB dynamic range B-mode images of the phantom depicted in Fig. 2 for three different transducer center frequencies: 10, 25, and 50 MHz, respectively. The white arrow in (c) indicates a dark spot that might have originated from nonabsorbing ambient medium.

the upper panel of Fig. 7 that boundary signals are very strong and signal amplitude approaches to zero outside the boundaries. Further, signal amplitude in the middle segment is reduced significantly. A similar observation can also be made from other panels. It is also interesting to note from the middle and lower panels that the height of the boundary signals has decreased and the signal amplitude outside the boundaries has become nonzero.

PA images generated at 10 MHz of a cylindrical region containing cells at volume fractions 0.1, 0.3, and 0.4 are shown in Figs. 8(a)–8(c), respectively. However, no cells are present outside this volume, meaning that light absorption does not take place. Fig. 8(a) illustrates that pixels at the boundaries of the cylindrical region are much brighter compared with that of the middle segment. This is because boundary signals are much stronger than that of the central region. The tiny signals from cells located close to each boundary add up in phase at the transducer surface and that results in boundary buildup. However, cells are randomly placed within the central region, and consequently phase variations are completely randomized between 0 and 2π. Therefore, incoherent addition takes place, leading to great reduction in signal strength. These effects are much more prominent for phantoms with higher concentrations of cells, as shown in Figs. 8(b) and 8(c). In other words, speckles are greatly suppressed in these cases. It is further clear from Fig. 8(d) where speckle visibility, defined as the square root of the average speckle power divided by the square root of the boundary power [34], is plotted as a function of cell concentration inside the cylindrical region. Fig. 8(d) shows that speckle visibility decreases with increasing cell concentration.

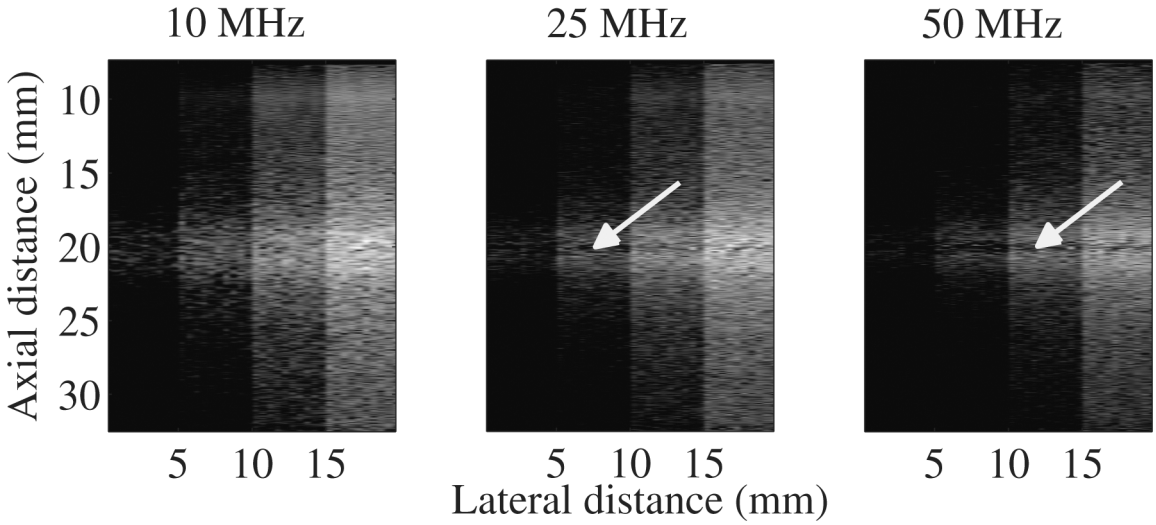

Fig. 5. 50 dB dynamic range B-mode PA images of a staircase phantom. Each stair step contains randomly located cells with fixed intracellular NP concentration as shown in Fig. 3(a). The cellular absorption coefficients (μ) are -20, -10, 0, and 10 dB, from left to right. (a)–(c) The three images correspond to three different transducer center frequencies: 10, 25, and 50 MHz, respectively. The white arrows in (b) and (c) indicate dark spots that may represent nonabsorbing extracellular matrix.

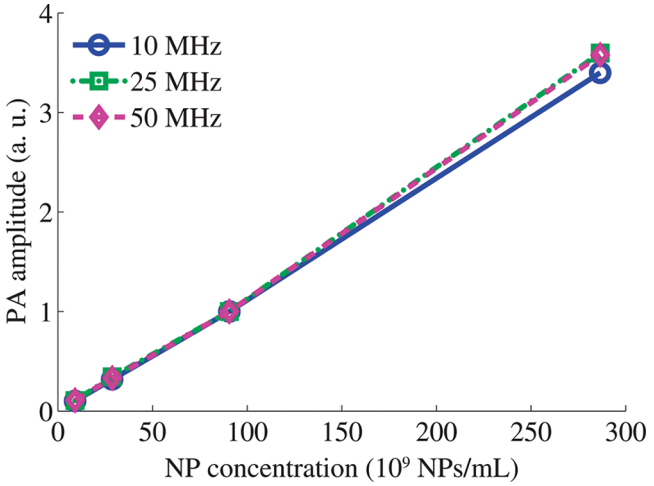

Fig. 6. Variation of average PA amplitude with NP concentration. NPs are inside the cells (9×10^9 to 286×10^9 NPs/mL corresponds to 4.5×10^4 to 143.2×10^4 NPs/cell). The average amplitude was obtained from an area of 4×10 mm on a stair step at the focal region of Fig. 5.

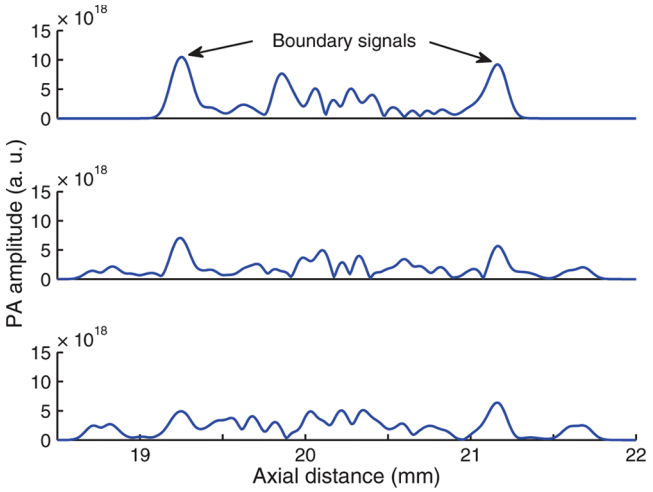

Fig. 7. Representative plots of A-lines corresponding to the central region of phantoms used for speckle studies (output of 10-MHz transducer). (a) Corresponds to the sample for which volume fraction occupied by cells within the cylinder is 20% but it is 0% outside [see Fig. 3(b)]. (b) The same quantity is about 20% within the enclosed region but it is 5% outside; cells in both the regions have the same μ values. (c) Cell concentration inside and outside the cylinder is identical and it is about 20%; μ for cells inside the cylinder is 2.5-fold higher than that of cells outside (i.e., contrast is 2.5).

The role of boundary buildup on speckle suppression is further elucidated in this study. Figs. 9(a)–9(c) present simulated PA images for a 10-MHz transducer of a cylindrical region populated with cells occupying a fixed volume fraction of 0.2, but with cellular volume fractions outside this region at 0, 0.05, and 0.1, respectively. Strong boundary buildup can be noticed in Fig. 9(a) and therefore, speckle visibility is less. However, the strength of the boundary signal is reduced as the cell concentration outside the cylindrical region increases [see Figs. 9(b) and 9(c)] and the associated speckle visibility increases. This is expected because signals from cells outside the cylindrical region and from cells situated close to boundary (and also inside the cylindrical region) may meet out of phase at the transducer surface, diminishing the boundary effect. Speckle visibility as a function of cell concentration outside the cylindrical region is quantified in Fig. 9(d).

It has also been studied in this work how intracellular NP concentration affects speckles in simulated PA images. In Figs. 10(a)–10(c), cell concentrations inside and outside the cylindrical region are the same (cellular volume fraction ≈0.2). Endocytosed NP concentration outside the cylindrical region is about 18.1×10^4, 4.5×10^4, and 2.3×10^4 NPs/cell in Figs. 10(a)–10(c), respectively. However, it is fixed at 45.3×10^4 NPs/cell within the cylindrical region in each figure. Accordingly, contrast can be computed to be 2.5, 10, and 20, respectively. It can be seen that boundary regions appear distinctly in each figure. Nevertheless, the boundary effect is more pronounced for samples with higher contrasts. PA signals from cells outside and inside the boundary do not differ significantly in Fig. 10(a) because contrast is less and therefore, signals of similar strengths interfere, causing a great reduction of the boundary effect. Moreover, the speckle pattern is approximately similar over the entire image. In the cases of Fig. 10(b) and 10(c), the interference effect close to boundary is not so dominant because the contrast is high, leading to strong boundary buildup. As expected, speckle visibility decreases as the contrast increases. Speckle visibility is quantitatively presented in Fig. 10(d). Guo *et al.* [34] also obtained a similar trend when constructing RF lines for a numerical phantom comprising large number of point sources (≈10^5 per wavelength).

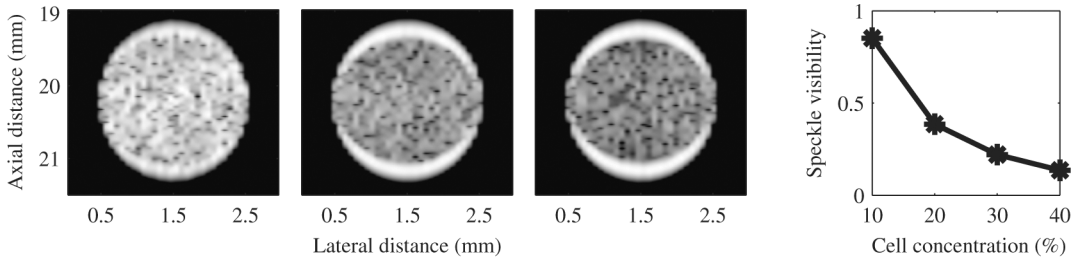

Fig. 8. (a)–(c) 30 dB dynamic range B-mode PA images generated with 10-MHz transducer. Volume fractions occupied by cells inside the circular region for (a)–(c) are about 10%, 30%, and 40%, respectively, but it is fixed at 0% outside. (d) Associated variation of speckle visibility as a function of cell concentration inside the circular region.

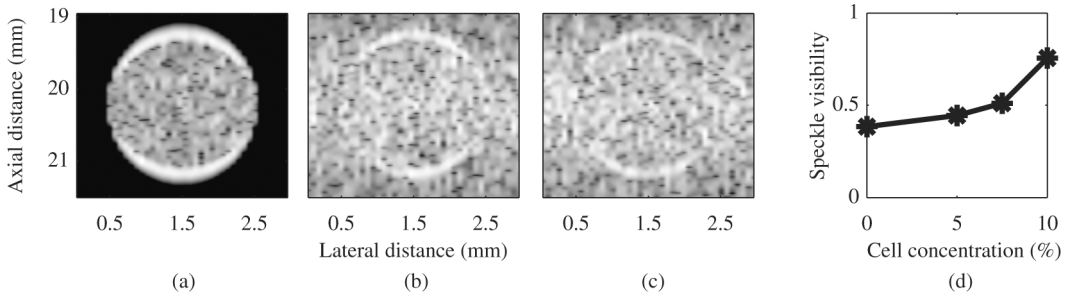

Fig. 9. (a)–(c) 30 dB dynamic range B-mode PA images generated with 10-MHz transducer. Volume fractions occupied by cells outside the circular region for (a)–(c) are about 0%, 5%, and 10%, respectively, but it is kept constant at 20% inside. (d) Corresponding variation of speckle visibility as a function of cell concentration outside the circular region.

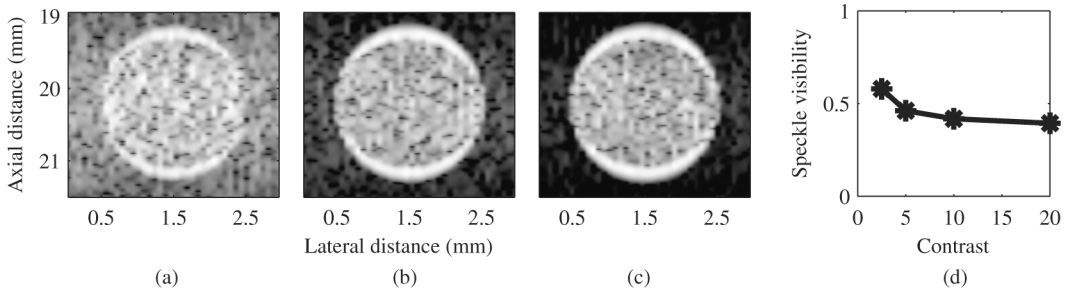

Fig. 10. (a)–(c) 30 dB dynamic range B-mode PA images generated with 10-MHz transducer. Volume fractions occupied by cells outside and inside the circular region are about 20%. The intracellular NP concentration for cells inside the circular region is about 45.3×10^4 NPs/cell in each figure. However, it is approximately 18.1×10^4, 4.5×10^4, and 2.3×10^4 NPs/cell in (a)–(c), respectively, for cells outside the circular region. (d) The variation of speckle visibility as a function of contrast.

V. Discussion and Conclusions

A theoretical framework is presented for PA image simulation of a collection of light-absorbing cells. This is similar to conventional ultrasound B-mode imaging of an ensemble of scatterers. It seems that this approach may be suitable for PA imaging of a medium composed of discrete absorbing structures. Additionally, effects of polydispersity in size and strength of absorbers, and other practical factors related to the receiver (such as geometry, apodization, etc.) can easily be incorporated in this framework. The simulation methodology presented in this paper has been utilized to simulate PA images of various numerical phantoms and to study the origin of speckles. Further, noise-free signals were considered in this study for simplicity. Nevertheless, in practice, PA signals are corrupted with noise, which is likely to alter speckle visibility. Intuitively, average boundary power would be reduced by the addition of zero-mean Gaussian noise to the boundary signal and, hence, speckle visibility would be enhanced. It would be interesting in future work to examine the effect of the Gaussian noise on speckle visibility in detail.

As stated earlier, the k-Wave method has been exclusively utilized for PA image simulations of regular objects as well as vascular structures. It has proved to be a very powerful tool for obtaining qualitative and quantitative insight into various parameters that influence PAT outcome. This method was also employed here to simulate images of some phantoms for comparison. For this purpose, a cylindrical region (radius 200 μm and height 50 μm) containing cells labeled with AuNPs was considered [see Fig. 3(b)]. This region was imaged using the approach presented in this manuscript with a transducer of diameter 135 μm and 25 MHz as the center frequency. Figs. 11(a)–11(c) represent such images when cells occupy 10%, 20%, and 30% of the cylindrical volume. As observed previously (see Fig. 8), boundary buildup increases as the cellular concentration increases, and also speckles are apparent at the internal regions. Images of equivalent effective media simulated with the k-Wave tool box are shown in Figs. 11(d)–11(f). The numerical values of effective parameters were obtained by exploiting the additive nature of various physical constants.[1] PA pressure data were evaluated over a 3-D spatial grid of $256 \times 128 \times 128$ pixels at a time step of approximately 1 ns. A perfectly matched layer of width 10 grid points was considered for boundary matching. Spatial resolution along each direction was chosen to be 5 μm. The circular boundary appears prominently in each figure, whereas the central region produces a very weak signal (PA amplitude below the lower cut off). The boundary effect is most pronounced for the medium in which cell concentration is maximum. Moreover, the imag-

[1] The density, compressibility, sound velocity, and light absorption coefficient for the effective medium (denoted by eff) were defined as $\rho_{\text{eff}} = (v_1\rho_s + v_2\rho_f)/V$, $\kappa_{\text{eff}} = (v_1\kappa_s + v_2\kappa_f)/V$, $c_{\text{eff}} = 1/\sqrt{\rho_{\text{eff}}\kappa_{\text{eff}}}$, and $\mu_{\text{eff}} = v_1\mu/V$, respectively. Here, v_1, v_2, and V are the total volume occupied by cells, volume of extracellular matrix, and volume of the illuminated region, respectively.

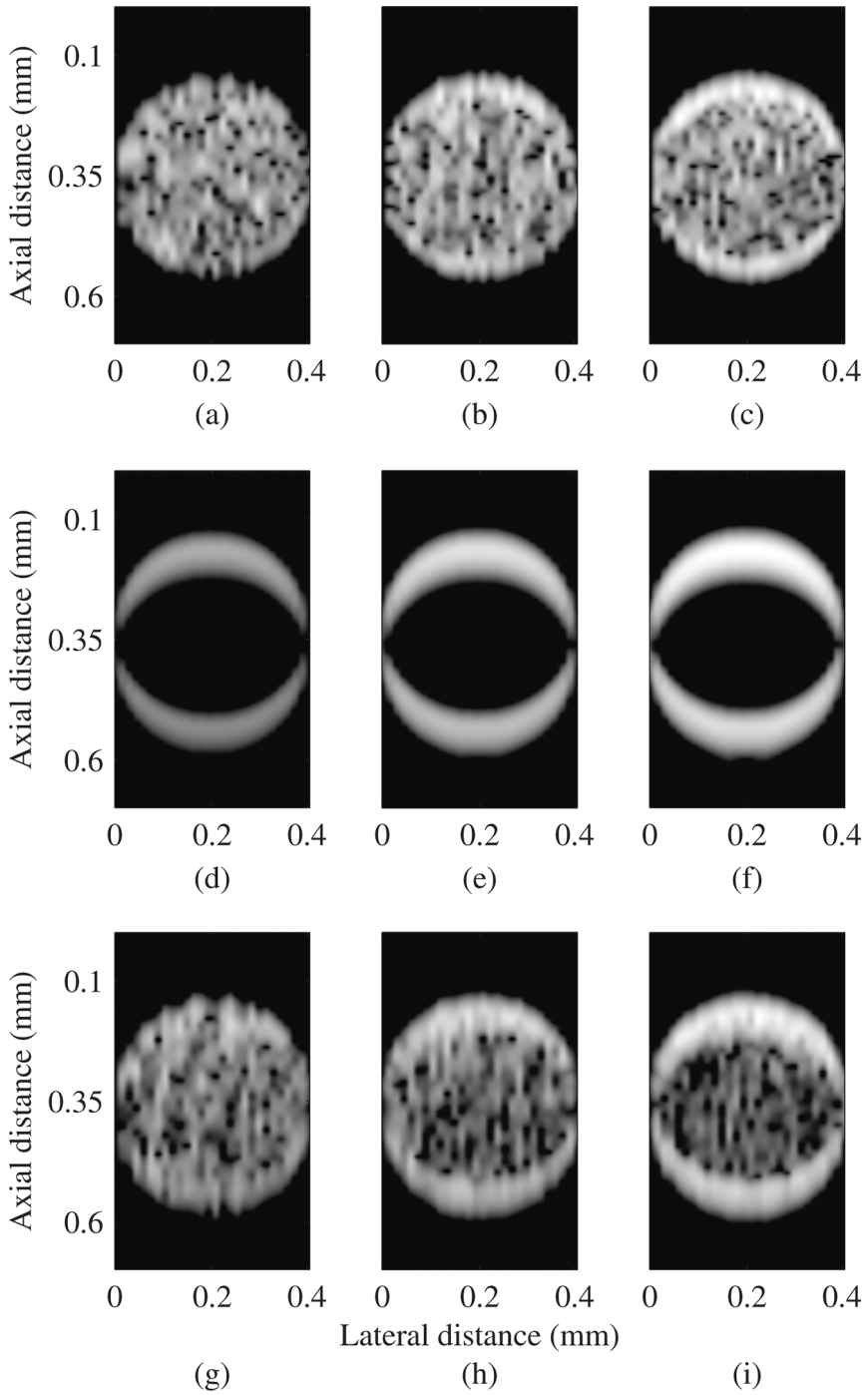

Fig. 11. (a)–(c) 30 dB dynamic range B-mode PA images generated with a 25-MHz transducer of diameter 135 μm employing the particle-based method discussed in this manuscript. Cellular volume fractions inside the cylinder are 0.1, 0.2, and 0.3, respectively. (d)–(f) Similar images of effective media simulated with the k-Wave method. (g)–(i) Images constructed with the k-Wave tool box when non-overlapping cells are randomly placed at the grid points inside the cylinder (grid resolution 5 μm).

es shown in Figs. 11(d)–11(f) seem to be speckle free. This is expected because the absorbing medium is assumed to be composed of freely suspended chromophores, as many k-Wave implementations assume [18], [19]. Therefore, the notion of confinement of chromophores [or discrete absorbers (cells)] and consequently, interference of signals emitted by absorbers, has been ignored. The structural details of the imaging medium at the micrometer level may be included in this method and their effects may be examined.

To study this aspect, cells were placed randomly under a non-overlapping condition at grid locations within the cylinder. The volume concentrations of cells inside the cylinder were taken to be 10%, 20%, and 30% for three different phantoms [the same phantoms were also used to generate Figs. 11(a)–11(c)]. The initial pressure was as-

signed to be nonzero ($\propto \mu$) at grid points enclosed by cells; otherwise, it was set to be zero. Final pressure data were obtained by deploying the k-Wave tool box. Corresponding images are displayed in Figs. 11(g)–11(i). The circular boundary appears distinctively in each figure. Most importantly, pixels in the central regions retain nonzero gray levels resulting in the appearance of speckle. This may be attributed to the fact that in this implementation, pressure waves from individual sources are allowed to interfere producing such a pattern, which is similar to that of Figs. 11(a)–11(c). Qualitative agreement between Figs. 11(a)–11(c) and Figs. 11(g)–11(i) indeed validates the methodology described in this paper. Further, the width of the circular boundary in a k-Wave image is wider than that of an image generated by the present approach (boundary width seems to be dictated by low-frequency content of the signal). It might be noted that the frequency contents of the initial simulated RF lines produced by the two methods were drastically different. For example, the maximum supported frequency in k-Wave lines was approximately 150 MHz, whereas it was 2000 MHz in the other case. In both cases, simulated RF lines were suitably downsampled and then filtered to generate B-mode images. However, it might be speculated that ultrahigh-frequency components of the current method might have influenced low-frequency content, leading to a narrower boundary than that of the k-Wave.

It might also be mentioned that k-Wave simulations were performed over a small spatial domain to restrict execution time within a practical limit. For instance, the generation of an image via k-Wave involved ≈9 h of computation. In contrast, the approach presented in this study takes advantage of analytical solutions to the PA wave equation for absorbers of regular shapes for constructing RF lines, and therefore reduces the computational burden significantly (e.g., it required a few minutes to simulate an image in the same computer). Finally, although the methodology described here is a computationally efficient technique, it is limited to absorbers with regular shapes only.

It is known that endocytosed NPs are confined within small vacuoles referred to as endosomes and their size may be up to 1 micrometer [14], [35], [36]. It is discussed in literature that NPs within endosomes may have plasmonic interaction because of close packing. Such an interaction may lead to temperature rise sufficient to alter thermophysical parameters, particularly at high fluence, and may contribute to nonlinear increase of PA amplitude with fluence. Nonlinear variation of PA amplitude with laser fluence was observed experimentally and also reported in literature (see [14, Fig. 4]). Nevertheless, in this work, plasmonic interaction between NPs was not taken into account and it might be a valid approximation for low fluence. Thus, the proposed methodology may not work at high laser fluence.

In conclusion, a theoretical model is described to simulate PA image of collection of cells labeled with AuNPs. A Monte Carlo algorithm was implemented to generate random locations of cells in 3-D. PA images were formed for a focused ultrasound transducer and at three center frequencies (10, 25, and 50 MHz). It was found that the approach faithfully imaged numerical phantoms used in this study. The origin of speckles in PA imaging was also investigated in this work. It was observed that speckles are greatly suppressed when absorbers are confined in a region (e.g., red blood cells in vessels). However, speckles become apparent when absorbers are not bounded to a region. Experimental validation of the observations reported in this study as well as implementation of this framework for array transducer involving dynamic focusing will form the subject matter of a separate investigation.

Acknowledgment

The authors are grateful to Dr. Manojit Pramanik, Indian Institute of Science, Bangalore, India, (now at Nanyang Technological University, Singapore) for stimulating discussion.

References

[1] P. Beard, "Biomedical photoacoustic imaging," *Interface Focus*, vol. 1, no. 4, pp. 602–631, 2011.

[2] H. F. Zhang, K. Maslov, G. Stoica, and L. V. Wang, "Functional photoacoustic microscopy for high-resolution and noninvasive *in vivo* imaging," *Nat. Biotechnol.*, vol. 24, no. 7, pp. 848–851, 2006.

[3] L. V. Wang and S. Hu, "Photoacoustic tomography: In vivo imaging of organelles to organs," *Science*, vol. 335, no. 6075, pp. 1458–1462, 2012.

[4] E. M. Strohm, E. S. L. Berndl, and M. C. Kolios, "High frequency label-free photoacoustic microscopy of single cells," *Photoacoustics*, vol. 1, no. 3–4, pp. 49–53, 2013.

[5] E. Filoux, A. Sampathkumar, P. V. Chitnis, O. Aristizábal, and J. A. Ketterling, "High frequency annular array with coaxial illumination for dual-modality ultrasonic and photoacoustic imaging," *Rev. Sci. Instrum.*, vol. 84, no. 5, art. no 053705, 2013.

[6] A. Needles, A. Heinmiller, J. Sun, C. Theodoropoulos, D. Bates, D. Hirson, M. Yin, and F. Stuart Foster, "Development and initial application of a fully integrated photoacoustic micro-ultrasound system," *IEEE Trans. Ultrason. Ferroelectr. Freq. Control.*, vol. 60, no. 5, pp. 888–897, 2013.

[7] R. A. Kruger, W. L. Kiser Jr., D. R. Reinecke, and G. A. Kruger, "Thermoacoustic computed tomography using conventional linear transducer array," *Med. Phys.*, vol. 30, no. 5, pp. 856–860, 2003.

[8] J. J. Niederhauser, M. Jaeger, R. Lemor, P. Weber, and M. Frenz, "Combined ultrasound and optoacoustic system for real-time high-contrast vacular imaging *in vivo*," *IEEE Trans. Med. Imaging*, vol. 24, no. 4, pp. 436–440, 2005.

[9] R. G. M. Kolkman, P. J. Brands, W. Steenbergen, and T. G. van Leeuwen, "Real-time *in vivo* photoacoustic and ultrasound imaging," *J. Biomed. Opt.*, vol. 13, no. 5, art. no. 050510, 2008.

[10] G. Xu, J. R. Rajian, G. Girish, M. J. Kaplan, J. B. Fowlkes, P. L. Carson, and X. Wang, "Photoacoustic and ultrasound dual-modality imaging of human peripheral joints," *J. Biomed. Opt.*, vol. 18, no. 1, art. no. 10502, 2013.

[11] J. Gateau, M. Á. A. Caballero, A. Dima, and V. Ntziachristos, "Three-dimensional optoacoustic tomography using a conventional ultrasound linear detector array: Whole-body tomographic system for small animals," *Med. Phys.*, vol. 40, no. 1, art. no. 013302, 2013.

[12] X. Yang, E. W. Stein, S. Ashkenazi, and L. V. Wang, "Nanoparticles for photoacoustic imaging," *Wiley Interdiscip. Rev. Nanomed. Nanobiotechnol.*, vol. 1, no. 4, pp. 360–368, 2009.

[13] S. Mallidi, P. P. Joshi, K. Sokolov, and S. Y. Emelianov, "On sensitivity of molecular specific photoacoustic imaging using plasmonic gold nanoparticles," in *Proc. Annu. Int. Conf. IEEE Engineering in Medicine and Biology Society*, 2009, pp. 6338–6340.

[14] S. Y. Nam, L. M. Ricles, L. J. Suggs, and S. Y. Emelianov, "Nonlinear photoacoustic signal increase from endocytosis of gold nanoparticles," *Opt. Lett.*, vol. 37, no. 22, pp. 4708–4710, 2012.
[15] M. Eghtedari, M. Motamedi, V. L. Popov, N. A. Popov, and A. A. Oraevsky, "Optoacoustic imaging of gold nanoparticles targeted to breast cancer cells," *Proc. SPIE*, vol. 5320, pp. 21–28, 2004.
[16] A. de la Zerda, C. Zavaleta, S. Keren, S. Vaithilingam, S. Bodapati, Z. Liu, J. Levi, B. R. Smith, T. Ma, O. Oralkan, Z. Cheng, X. Chen, H. Dai, B. T. Khuri-Yakub, and S. S. Gambhir, "Carbon nanotubes as photoacoustic molecular imaging agents in living mice," *Nat. Nanotechnol.*, vol. 3, no. 9, pp. 557–562, 2008.
[17] B. Cox and P. C. Beard, "Modeling of photoacoustic propagation in tissue using k-space techniques," in *Photoacoustic Imaging and Spectroscopy*, L. V. Wang, Ed., London, UK: Taylor & Francis, 2009, pp. 25–34.
[18] B. E. Treeby and B. T. Cox, "k-Wave: MATLAB toolbox for the simulation and reconstruction of photoacoustic wave fields," *J. Biomed. Opt.*, vol. 15, no. 2, art. no. 021314, 2010.
[19] C. B. Shaw, J. Prakash, M. Pramanik, and P. K. Yalavarthy, "Least-sqares QR-based decomposition an efficient way of computing and optimal regularization parameter in photoacoustic tomography," *J. Biomed. Opt.*, vol. 18, no. 8, art. no. 80501, 2013.
[20] G. J. Diebold, T. Sun, and M. I. Khan, "Photoacoustic monopole radiation in one, two and three dimensions," *Phys. Rev. Lett.*, vol. 67, no. 24, pp. 3384–3387, 1991.
[21] R. K. Saha and M. C. Kolios, "A simulation study on photoacoustic signals from red blood cells," *J. Acoust. Soc. Am.*, vol. 129, no. 5, pp. 2935–2943, 2011.
[22] K. K. Shung and G. A. Thieme, *Ultrasound Scattering in Biological Tissues*. Boca Raton, FL: CRC Press, 1993.
[23] A. Ishimaru, *Wave Propagation and Scattering in Random Media*. New York, NY: Academic, 1978, pp. 69–92.
[24] E. Hysi, R. K. Saha, and M. C. Kolios, "On the use of photoacoustics to detect red blood cell aggregation," *Biomed. Opt. Express*, vol. 3, no. 9, pp. 2326–2338, 2012.
[25] R. K. Saha and M. C. Kolios, "Effects of erythrocyte oxygenation on optoacoustic signals," *J. Biomed. Opt.*, vol. 16, no. 11, art. no. 115003, 2011.
[26] R. K. Saha, S. Karmakar, and M. Roy, "Computational investigation on the photoacoustics of malaria infected red blood cells," *PLoS ONE*, vol. 7, no. 12, art. no. e51774, 2012.
[27] R. K. Saha, "Computational modeling of photoacoustic signals from mixtures of melanoma and red blood cells," *J. Acoust. Soc. Am.*, vol. 136, no. 4, pp. 2039–2049, 2014.
[28] R. K. Saha, M. Roy, and A. Datta, "Simulation study on the photoacoustics of cells with endocytosed gold nanoparticles," *Curr. Sci.*, vol. 106, no. 11, pp. 1554–1559, 2014.
[29] J. A. Jensen, "Linear description of ultrasound imaging systems," in *Notes Int. Summer School on Advanced Ultrasound Imaging*, 1999.
[30] P. K. Jain, K. S. Lee, I. H. El-Sayed, and M. A. El-Sayed, "Calculated absorption and scattering porperties of gold nanoparticles of different size, shape and composition: Applications in biological imaging and biomedicine," *J. Phys. Chem. B*, vol. 110, no. 14, pp. 7238–7248, 2006.
[31] P. B. Jhonson and R. W. Christy, "Optical constants of the noble metals," *Phys. Rev. B*, vol. 6, no. 12, pp. 4370–4379, 1972.
[32] O. Falou, M. Rui, A. E. Kaffas, J. C. Kumaradas, and M. C. Kolios, "The measurement of ultrasound scattering from individual micron-sized objects and its amplication in single cell scattering," *J. Acoust. Soc. Am.*, vol. 128, no. 2, pp. 894–902, 2010.
[33] M. Arditi, F. S. Foster, and J. W. Hunt, "Transient fields of concave arrays," *Ultrason. Imaging*, vol. 3, pp. 37–61, 1981.
[34] Z. Guo, L. Li, and L. V. Wang, "On the speckle-free nature of photoacoustic tomography," *Med. Phys.*, vol. 36, no. 9, pp. 4084–4088, 2009.
[35] C. Bao, N. Beziere, P. del Pino, B. Pelaz, G. Estrada, F. Tian, V. Ntziachristos, J. M. de la Fuente, and D. Cui, "Gold nanoprism as optoacpoustic signal nanoamplifiers for in vivo bioimaging of gastrointestinal cancers," *Small*, vol. 9, no. 1, pp. 68–74, 2013.
[36] A. Astolfo, F. Arfelli, E. Schültke, S. James, L. Mancini, and R.-H. Menk, "A detailed study of gold-nanoparticle loaded cells using X-ray based techniques for cell-tracking applications with single-cell sensitivity," *Nanoscale*, vol. 5, no. 8, pp. 3337–3345, 2013.

Subhajit Karmakar was born in Bankura, West Bengal, India, in 1978. He completed a B.Sc. degree in physics from Bankura Christian College in 1999 and subsequently received an M.Sc. degree in physics from The University of Burdwan in 2001. In 2002, he joined the Saha Institute of Nuclear Physics as a research scholar to work in ultrasound imaging. He obtained a Ph.D. degree from the University of Calcutta in 2013 for his work on signal processing. He also worked in photoacoustic tissue characterization as a senior research fellow at the Saha Institute of Nuclear Physics from 2011 to 2013. He joined the University Science Instrumentation Centre of the University of Burdwan in 2013 as a senior scientific officer. His research interests include signal processing, human–computer interaction, photoacoustic imaging, and simulations.

Madhusudan Roy obtained his B.Sc. degree in physics from the University of Calcutta, Kolkata, India, in 1980. He obtained his M.Sc. and Ph.D. degrees in physics in 1982 and 1989, respectively, from the University of North Bengal, Darjeeling, India. He worked as a Research Associate in the Department of Spectroscopy, Indian Association for the Cultivation of Science, Kolkata, India. During his stay at the Indian Association for the Cultivation of Science, he studied photoreaction dynamics of some organic compounds using laser Raman spectroscopy. Then, he joined the North-Eastern Hill University, India, as a Lecturer in physics in 1989. In 2002, he joined the Microelectronics Division, Saha Institute of Nuclear Physics, Kolkata, and is currently in the Surface Physics and Material Science Division of the Saha Institute of Nuclear Physics. He took part in many interdisciplinary research activities. He took initiatives to conduct experiments to study ultrasonic properties of some biophantoms. His current research interests lie in the development of gas sensors, synthesis and characterization of nanocomposites, photoacoustics, and the source of air pollutants and their physical and magnetic characterization.

Ratan K. Saha obtained his B.Sc. degree in physics from the University of North Bengal, Siliguri, India, in 1996 and M.Sc. degree in physics from Jadavpur University, Kolkata, India, in 1999. He carried out his Ph.D. work at the Saha Institute of Nuclear Physics, Kolkata, from 2000 to 2006. He worked as a postdoctoral fellow at the Laboratory of Biorheology and Medical Ultrasonics, Research Center of the University of Montreal Hospital, Montreal, Canada, from 2007 to 2008, in the Department of Physics, Ryerson University, Toronto, Canada, from 2009 to 2011, and the Saha Institute of Nuclear Physics from 2011 to 2013. Since October 2013, he has been a CSIR Pool Officer at the Saha Institute of Nuclear Physics. His current research interests include characterization and imaging of soft tissues using ultrasonics and photoacoustics.